

Flow-induced vibration control of a circular cylinder using rotational oscillation feedback

D. Vicente-Ludlam¹, A. Barrero-Gil^{1,†} and A. Velazquez¹

¹Department of Fluid Mechanics and Aerospace Propulsion, Universidad Politecnica de Madrid, Madrid, 28040, Spain

(Received 19 October 2017; revised 1 February 2018; accepted 14 April 2018;
first published online 21 May 2018)

The effect of imposed rotation on a slender elastically mounted circular cylinder free to oscillate transversely to the incident flow has been studied experimentally in a free-surface water channel. Rotation rate and direction are imposed to be proportional to either the cylinder's transverse displacement or the cylinder's transverse velocity to determine the effectiveness of these rotation laws to control the dynamics of the cylinder, either to reduce or to enhance oscillations. The former can be of interest for energy harvesting purposes whereas the latter can be useful to avoid unwanted oscillations. In all cases, non-dimensional mass and damping are fixed ($m^* = 11.7$, $\zeta = 0.0043$) so the analysis is focused on the role of the rotation law and the reduced velocity. The Reynolds number based on the diameter of the cylinder ranges from 1500 to 10 000. Results are presented in terms of steady-state oscillation characterization (say, amplitude and frequency) and wake-pattern topology, which was obtained through digital particle image velocimetry. Both laws are able to either reduce or enhance oscillations, but they do it in a different way. A rotation law proportional to the cylinder's displacement is more effective to enhance oscillations. For high enough actuation, a galloping-type response has been found, with a persistent growth of the amplitude of oscillations with the reduced velocity that shows a new desynchronized mode of vortex shedding. On the other hand, a rotation law proportional to the cylinder's transverse velocity is more efficient to reduce oscillations. In this case only vortex-induced-type responses have been found. A quasi-steady theoretical model has been developed, which helps to explain why a galloping-type response may appear when rotation is proportional to cylinder displacement and is able to predict reasonably the amplitude of oscillations in those cases. The model also explains why a galloping-type response is not expected to occur when rotation is proportional to the cylinder's velocity.

Key words: aerodynamics, flow–structure interactions

1. Introduction

Flow-induced vibrations (FIV) of elastic bodies occur somewhat frequently. They take place in a large variety of physical and biological systems, like airplane wings, leaves of trees, long-span bridges, tall buildings, heat exchange devices, clarinet reeds

[†] Email address for correspondence: antonio.barrero@upm.es

or offshore structures, to name only a few. Such FIV can cause both severe (even destructive) vibrations and beneficial motions. The fluid flow and the elastic response of the body are coupled, since the fluid force causes the body to deform and, as the body deforms, its orientation to the flow changes and so does the fluid force. The interaction between the moving body and the fluid flow is very complex and depends on a large number of parameters related to the fluid flow characteristics (among them flow velocity, fluid density and viscosity, turbulence of the inflow), structural (mechanical) properties of the body (mass, stiffness and mechanical damping) and geometry (shape of the body, surface roughness, etc.). Understanding the fluid–elastic coupling is of interest from both the scientific and the practical sides. Regarding the practical side, a new field of interest has recently emerged since FIV are being considered as a means to extract energy from fluid flows. As proposed by Bernitsas *et al.* (2008), a device called VIVACE (acronym for vortex-induced vibration aquatic clean energy) was developed to extract energy from water currents by oscillations induced by vortex shedding from a spring-mounted circular cylinder. Additional efforts have been made later in this direction, namely, Sanchez-Sanz, Fernandez & Velazquez (2009), Barrero-Gil, Pindado & Avila (2012), or Grouthier, Michelin & de Langre (2013). There have been other initiatives to extract energy efficiently, taking advantage of other FIV phenomena, like galloping (Barrero-Gil, Sanz-Andres & Alonso 2010; Abdelkefi, Hajj & Nayfeh 2012, 2013; Vicente-Ludlam, Barrero-Gil & Velazquez 2014), wake galloping (Jung & Lee 2011) or flutter (Doaré & Michelin 2011; Singh, Michelin & De Langre 2012).

There is a large variety of FIV phenomena but, broadly speaking, two different classes constitute the basis for the analysis of many related problems. The first one is vortex-induced vibration (VIV), which is caused by a nonlinear resonance phenomenon. For Reynolds number Re high enough (say, larger than 50), the flow separates from the body surface, generating an unsteady broad wake, where large-scale vortices are shed periodically from the body surface, leading to an alternating fluid force on the body. The shedding frequency of the vortices is related to the undisturbed flow speed and the size and shape of the body as shown by Strouhal (1878). When the frequency of the vortex shedding is close enough to the natural frequency of oscillation of the elastic body, a close-to-resonance condition is achieved and significant oscillations in the body can appear when the mechanical properties of the body (such as damping) are appropriate. VIV has been widely investigated, both experimentally and numerically, mainly through the canonical problem of a spring-mounted rigid circular cylinder under the action of a uniform fluid flow. Usually, the main interest has been focused on assessing the effect of different mechanical and fluid parameters on the VIV response: steady-state oscillations (amplitude and frequency), fluid forces on the cylinder, or flow pattern in the wake. For a detailed review, the reader is referred to Blevins (1990), Sarpkaya (2004, 2010), Williamson & Govardhan (2004), Bearman (2011) or Paidoussis, Stuart & De Langre (2011).

The other canonical problem that should be cited here is galloping (Parkinson 1989). This is a motion-induced instability that appears in elastic bluff bodies with certain geometrical shapes – non-axisymmetric cross-sections like square, D-section, triangular or H-type (Naudascher & Rockwell 1994) – when the velocity of the incident flow exceeds a critical value. Then, a small transverse displacement of the body induces an angle of attack relative to the incoming flow and an asymmetric pressure distribution, so that fluid force appears in the direction of the displacement in such a way that energy is transferred from the flow to the body and oscillatory motion

(mainly transversely to the unperturbed flow) develops. Unlike VIV, which typically occurs only in a certain range of flow velocities and with self-limited amplitude, galloping takes place for any value of the flow velocity higher than the critical value and has a monotonic increase of amplitude with flow velocity. Galloping is mainly driven by the instantaneous angle of attack between the body and the incoming flow and does not necessarily need a synchronization between the oscillations and vortex formation and shedding.

As said earlier, VIV of a circular cylinder has been much studied in the past, due to the extensive use of cylindrical elements in structures and engineering systems as well as its interest from the scientific side. Most of these studies considered the conceptually simple case of an elastically mounted rigid cylinder (Sarpkaya 2010). Recently, an imposed asymmetry effect in the VIV of a spring-mounted circular cylinder was numerically studied at $Re = 100$ by Bourguet & Jacono (2014). The cylinder was free to oscillate transversely to the flow over a wide range of reduced velocities. In addition, rotation of the cylinder around its axis, with fixed direction of rotation and fixed rotation rate, was imposed. The cylinder was subject to VIV-type vibrations up to rotation rates of $\alpha = 4$ (α is the non-dimensional rotation rate, defined as the ratio of rotational velocity at the cylinder's surface to the unperturbed flow velocity). Oscillations increase with α as well as the region of synchronization where oscillations are significant up to a non-dimensional rotation rate close to $\alpha = 4$. Notoriously, they also reported a wake mode composed of a triplet of vortices and a single vortex per cycle (T+S wake mode) for some specific non-dimensional rotation rates and reduced velocity, which had not been previously reported in the literature on non-rotating cylinders in VIV. Seyed-Aghazadeh & Modarres-Sadeghi (2015) experimentally studied this same problem for Reynolds number between 350 and 1000, concluding that the lock-in regime got narrower at high rotation rates and oscillations ceased beyond $\alpha = 2.4$. When the cylinder is also allowed to oscillate along the in-line direction, Stansby & Rainey (2001) reported large oscillations with amplitudes higher than 10 diameters, with low-frequency galloping-like responses occurring without lock-in.

Another category deals with imposed combined translational and rotational oscillation. Blackburn, Elston & Sheridan (1999) were able to generate thrust in quiescent fluid by imposing combined translational and rotational oscillation. Nazarinia *et al.* (2009a,b) extended this study and experimentally characterized the flow around a circular cylinder undergoing imposed combined translational and rotational motion in a free stream, obtaining new interesting wake modes. Al-Mdallal (2004), Kocabiyik & Al-Mdallal (2005) and Nazarinia *et al.* (2009a) showed the possibility of reducing the synchronization region of the cylinder's motion in the near wake through the effect of the phase shift, velocity ratios and motion frequency of the translational and rotational modes. Finally, cited here should be experiments made considering rotational oscillations of a circular cylinder at rest in order to avoid vortex shedding using flow velocity in the wake as a feedback control variable (Fujisawa, Kawaji & Ikemoto 2001). More recently, Lu *et al.* (2011) linked the rotary oscillation of the cylinder to the fluctuating lift fluid force coefficient as an active control strategy for lift force reduction.

In the above-mentioned studies, the rotation imposed to the cylinder is not linked to the dynamics of the cylinder, and therefore is not coupled with the result of the fluid-elastic interaction. Recently, we thought that it could be of interest to link the rotation direction and rate to the oscillating cylinder dynamics, to see if this could be a method to reduce or enhance oscillations. Note that this is a full active

control technique where imposed rotation takes the cylinder dynamics as a feedback. To study this question, we carried out two-dimensional (2D) numerical simulations at low Reynolds number (Vicente-Ludlam *et al.* 2017) and investigated how the selected strategy for the cylinder's rotation, proportional to either the cylinder's transverse displacement (with respect to the static, without flow, cylinder position) or its velocity, affects the cylinder's response. It was found that, depending on the law of rotation, oscillations could be significantly increased or decreased with respect to the non-rotating cylinder. This result can be of applied interest, either to protect cylindrical structures (by diminishing oscillations) or to extract energy from the fluid flow (by enhancing oscillations). It was also found that, for certain cases of the rotating law proportional to the cylinder's displacement, a galloping-type response was observed, and a quasi-steady theoretical model can reasonably predict the amplitude of oscillation for these cases.

The Reynolds number in the numerical simulations that we carried out was 100. However, in many actual applications, 2D numerical simulations at $Re = 100$ might not be accurate enough and significant differences may appear for higher Reynolds numbers. The VIV response at low Reynolds numbers (laminar flow regime) is characterized by a two-branch curve, which presents a maximum amplitude of non-dimensional oscillations of $A^* \approx 0.6$. The branches appearing are usually classified as the initial branch and the lower branch. The initial branch corresponds to the initial reduced velocities where oscillations start. The vortex pattern in the near wake is characterized by a 2S mode (single vortex being shed per half-cycle of oscillations). After the initial-to-lower branch transitions, the maximum amplitude is obtained. The lower branch exhibits a C (2S) mode of vortex emission, where single vortices are shed per half-cycle and downstream they appear to coalesce (Pras Nath & Mittal 2008; Vicente-Ludlam *et al.* 2017). On the other hand, for larger Reynolds numbers, the response is characterized by a three-branch curve. They are classified as the initial, upper and lower branches (Williamson & Govardhan 2004). The upper branch appears in the transition between the initial and lower branches and is the region within the VIV curve with largest amplitude of oscillation. With respect to the modes of vortex emission, similarly to the low-Reynolds-number regime, the initial branch is composed of a 2S mode of vortex emission. Alternatively, the lower branch presents a 2P mode of vortex emission where a pair of vortices (with opposite rotation direction) is shed per half-cycle of oscillation. The upper branch presents a $2P_0$ mode, where a pair of vortices is shed per half-cycle, but the secondary vortex is much smaller than the primary one (Morse & Williamson 2009).

The Reynolds number, in addition to determining whether the upper branch appears or not, also influences the maximum amplitude of oscillations, which increases with Reynolds number as shown by Govardhan & Williamson (2006). They found that the maximum amplitude of oscillations appears to be governed by the mass-damping parameter as well as the Reynolds number. The differences found in classic (non-rotating) VIV of a circular cylinder due to Reynolds number encourage us to extend the numerical simulations presented in Vicente-Ludlam *et al.* (2017), and to see the extent to which the results found in the idealized numerical simulations (2D flow, uniform incoming flow, pure transverse motion of the cylinder, fixed Reynolds number) occur in experiments, in a larger Reynolds-number regime and with an experimental set-up closer to potential applications. Therefore, we have experimentally studied the idea of imposing a rotation in the cylinder axis (linked to its dynamics), with a Reynolds number in the range of 1500–10 000 (between one and two orders of magnitude higher than the computational studies we presented

in Vicente-Ludlam *et al.* (2017)). During experiments, an active control of cylinder rotation in real time, with low enough time lag, that closely follows the cylinder transverse position/velocity was implemented. When rotation was proportional to the cylinder's transverse displacement, significant changes in the response were found with respect to the non-rotating case. Depending on the sign of the constant of proportionality between rotation and cylinder displacement, the oscillations were diminished or significantly enhanced. In the latter case, even a galloping-type response appeared when the forced rotation is greater than a certain level. When the cylinder rotates proportionally to the cylinder's transverse velocity, it is possible to increase or diminish oscillations but the response always has a vortex-induced type (resonant) character.

This article is organized as follows. In §2, the experimental set-up is described, including a description of the recirculating water channel where experiments have been performed as well as a description of the particle image velocimetry (PIV) set-up used to characterize the flow field of the near wake of the oscillating cylinder. Also, validation tests of the water channel are given by comparing VIV results of a non-rotating circular cylinder to similar ones published in the literature. In §3, flow-induced vibration results for the cylinder with prescribed rotatory law proportional to the cylinder's position are presented first. A quasi-steady theoretical model has been developed and presented which can reasonably predict the amplitude of oscillation for these cases (galloping-type response). Afterwards, the results for the cylinder with a rotation law proportional to the cylinder's velocity are presented. The quasi-steady model helps to explain why a galloping-type response is not expected to occur in this case. For each of the rotation laws investigated, vorticity contour maps obtained through PIV measurements have been presented and discussed. Finally, concluding remarks are presented in §4. Additionally, in the supplementary material associated with this article, movies displaying oscillations in experiments with different rotating laws are presented at <https://doi.org/10.1017/jfm.2018.332>.

2. Experimental set-up and validation

2.1. Experimental set-up

The experiments were carried out in a free-surface recirculating water channel with controlled inflow conditions at the test section in terms of mean speed, uniformity and low turbulence. A sketch of the water channel is given in figure 1. The water current is driven by two axial pumps manufactured by ABS, model RCP 500. The rotation speed of the pumps is regulated by a variable-frequency drive from Power Electronics, model SD503942. Guide vanes are placed in the corners of the water channel to guide the flow and reduce pressure losses. To improve flow quality in the test section, a honeycomb (hexagonally shaped cells with diameter 4.5 mm and a length-to-diameter ratio of 12) and a fine screen are located before the entrance of the test section. As is known, the honeycomb is a very effective flow-straightening device (as shown by Bradshaw & Pankhurst (1964)) and the screen is effective to reduce mean non-uniformities and fluctuations of the streamwise component. During experiments, the flow speed U at the test section was varied between 75 and 480 mm s⁻¹, which gives a Reynolds-number range of $Re = UD/\nu \approx 1500\text{--}10\,000$, ν being the kinematic viscosity of the water and D the cylinder diameter. With respect to the inflow conditions, the turbulence intensity was lower than 1.5% and the velocity uniformity presented variations lower than 5% throughout the test section studied. Further details regarding the water channel can be found in Xu-Xu, Barrero-Gil & Velazquez (2016).

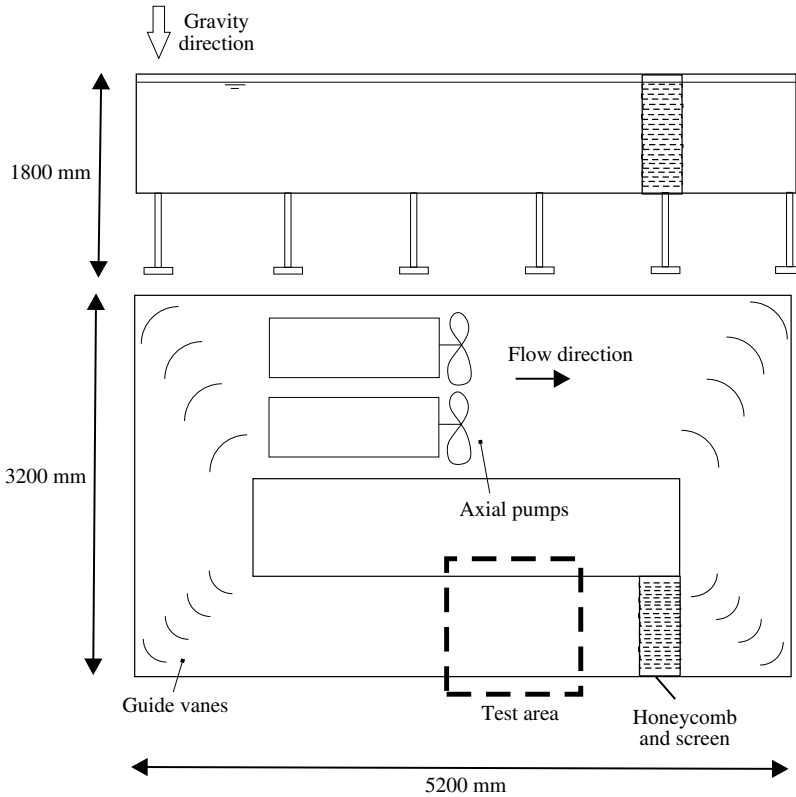


FIGURE 1. Schematic elevation and plan of the free-surface water channel.

The test section is 3000 mm in length, 900 mm in width and the working depth is 830 mm (A; see figure 2a). The test section is made of glass, which allows the flow to be viewed from either side, as well as from the bottom, allowing one to perform flow visualizations through PIV measurements. A circular cylinder (B), made of aluminium, of diameter $D = 25$ mm and immersed length $L = 430$ mm, was attached through a bearing (C) to the shaft of a servomotor (D) fixed to the free end of a double-blade elastic system. The elastic system, which follows the arrangement introduced in Assi *et al.* (2006), was made up of two parallel rigid aluminium blocks (E), coupled to a pair of thin spring-steel flexor blades (F). The elastic system not only acts as the cylinder support, but also provides the linear restoration response. In this way, the cylinder is restricted to oscillate in the transverse direction to the flow (y) with low mechanical damping. Figure 2(b) presents a detailed view of the flexors and elastic system, including the servomotor attached to it. The transverse displacement and acceleration of the circular cylinder were measured by a non-contact laser vibrometer (G) from Aquity AR500-500 (range 500 mm, resolution 0.05 mm) and by an accelerometer (H) from Measuring Specialities (range ± 2 g, resolution 2 mg).

An AC servomotor, 60ST-M013330C from MIGE, with a peak torque of 3.9 N m and a maximum rated speed of 3000 r.p.m., was used. To measure the angle of rotation, the servomotor includes a photoelectric encoder with resolution of 0.036° . To impose the rotation law, a signal command was sent to the servomotor controller.

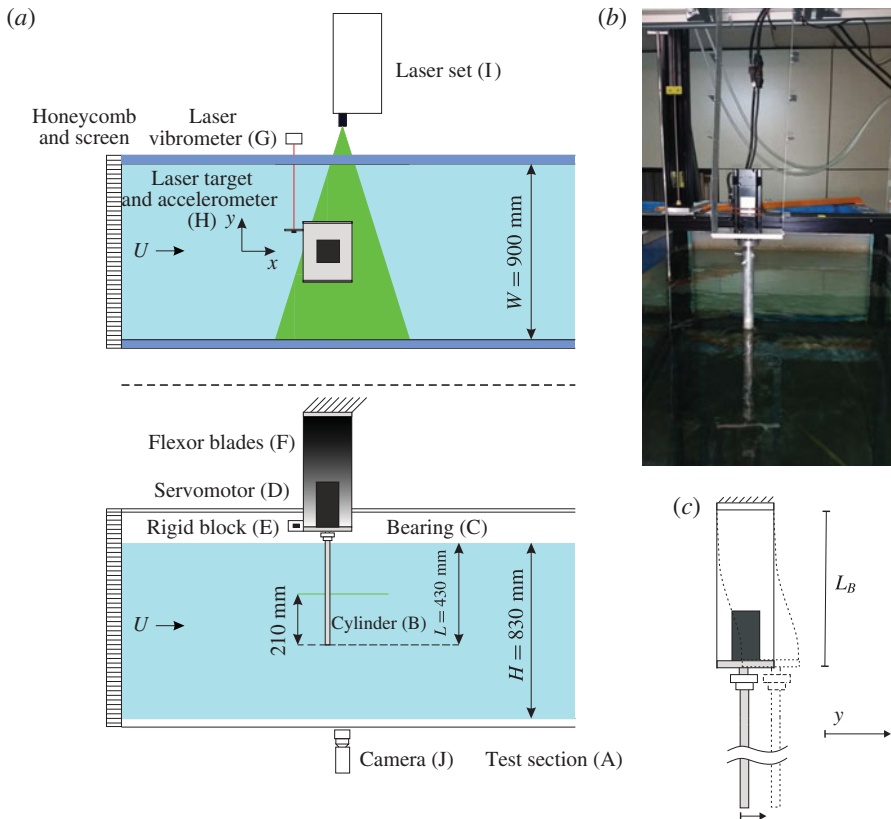


FIGURE 2. (Colour online) Sketch of the experimental set-up (dimensions are in millimetres). (a) Schematic top view and side view of the water channel. (b) Photograph of a close view of the elastic system. (c) Detail of the elastic system's deformation when a translation in the transverse direction is applied.

Depending on the rotation law, this signal command was proportional either to the cylinder's position (measured with the laser vibrometer) or to the cylinder's velocity (obtained by integration of the accelerometer's signal). The time delay between the servomotor response and the signal command was under 5 ms, which is much smaller than the characteristic oscillation times during the experiments (a maximum phase lag of 1.5° was observed). The cylinder was connected to the shaft of the servomotor through a bearing manufactured at our installations. Before each run, parallelism of the cylinder as well as dynamic balancing was checked through measurements of the accelerometer installed.

All data (position, acceleration, rotation angle) were recorded and registered using a Compact-Rio microprocessor from National Instruments (NI cRio-9024) and an analogue input module from National Instruments (± 10 V, NI-9201) with a sampling frequency of 200 Hz for each parameter combination of flow velocity and prescribed rotation law for a total of 16 minutes. The first 6 minutes were spent achieving steady-state conditions while the remaining 10 minutes were used for recording. After that, the water speed was increased and the measurement procedure repeated.

2.2. Data reduction and rotation laws evaluated

For each run, the instantaneous transverse position $y(t)$ around the static (no-flow) position, acceleration $\ddot{y}(t)$ and rotation angle $\theta(t)$ of the cylinder were directly measured and registered. The dynamical equation of the cylinder and the rotation laws employed are, respectively,

$$m\ddot{y} + c\dot{y} + ky = -m_A\ddot{y} + \frac{1}{2}\rho U^2 DLC_y, \quad (2.1a)$$

$$\theta = k_1 y \quad \text{or} \quad \theta = k_2 \dot{y}, \quad (2.1b,c)$$

where m is the total oscillating mass, c is the mechanical damping constant, k is the stiffness of the system, and k_1 and k_2 are feedback constants, which relate the rotation to be imposed on the cylinder and the displacement/velocity of the cylinder, respectively. Both c and k were measured in free decay tests in still air. Regarding the right-hand side of (2.1a), note that the fluid force has been split into two terms, a potential added-mass term ($-m_A\ddot{y}$) and a viscous one ($\rho U^2 DLC_y/2$), as suggested in Govardhan & Williamson (2000); ρ is the fluid density, and C_y is a dimensionless fluid force coefficient.

Equation (2.1b,c) shows the two rotation laws that have been tested in order to determine how such rotation affects the VIV response of the cylinder; in particular, (i) the cylinder is rotated proportionally to its transverse displacement and (ii) the cylinder is rotated proportionally to its transverse velocity.

The equation of motion of the cylinder and the rotation laws prescribed can be made dimensionless by introducing D and $f_N^{-1} = ((m + m_A)/k)^{1/2}$ as reference length and time scales. This gives

$$Y'' + 4\pi\zeta Y' + 4\pi^2 Y = \frac{2U^{*2}}{\pi(m^* + C_A)} C_y, \quad (2.2a)$$

$$\theta = \tilde{k}_1 Y \quad \text{or} \quad \theta = \tilde{k}_2 Y', \quad (2.2b,c)$$

where $Y = y/D$, $\zeta = c/[2(k(m + m_A))^{1/2}]$ is the damping ratio, $m^* = m/(\rho D^2 L)$ is the mass ratio, C_A is the potential added-mass coefficient ($C_A = 1.0$ for a circular cylinder), $\tilde{k}_1 = Dk_1$ and $\tilde{k}_2 = f_N Dk_2$ are the non-dimensional feedback constants, and the prime stands for differentiation with respect to non-dimensional time $t^* = f_N t$.

A standard method of analysis employed for the study of FIV problems is based on the introduction of time-averaged quantities (Sarpkaya 2004). The following variables were computed from each run: (i) the steady-state normalized maximum amplitude of oscillation $A^* = A_{10}/D$, where A_{10} denotes the maximum 10% peaks of oscillation for each run; (ii) the normalized frequency of oscillations $f^* = f/f_N$, where the frequency of oscillations f was computed from the fast Fourier transform of $y(t)$.

2.3. Particle image velocimetry measurements

The PIV set used to characterize the flow field of the near wake of the cylinder was from Dantec Dynamics. Flow illumination was provided by a pulsed Nd:YAG 800 mJ laser. Each laser pulse lasted for 5 μ s. Images were taken using a Dantec Dynamics Flow Sense 2ME camera with a resolution of 1600 pixels \times 1200 pixels. Data transmission was made directly to the PC RAM via a PCIe-1427 image acquisition board, which allows for an information transfer greater than 200 MB per second. The camera lens was a Zeiss Makro-Planar T 2/50 mm ZF. The laser sheet intercepts the circular cylinder perpendicular to its axis at a height of 210 mm from its bottom end. After passing through the sidewalls, it was verified that the thickness of the laser sheet was smaller than 1 mm. The camera was set under the water channel

perpendicular to the laser sheet. The flow was seeded with hollow glass spheres having a diameter of $10\ \mu\text{m}$ (HGS-10). Synchronization between image capturing and flow illumination and the analysis was carried out using the Dynamic Studio Dantec software.

PIV measurements were carried out with the laser sheet perpendicular to the circular cylinder at a constant height of 210 mm from the bottom end of the cylinder with the camera situated under the water channel (oriented perpendicular to the laser sheet; see figure 2a). The field of view of the camera corresponds approximately to a rectangle of $9D \times 6.75D$ that has physical dimensions of 225 mm \times 169 mm containing 1600 pixels \times 1200 pixels and focuses on the near wake after the circular cylinder.

Sampling of the flow field was carried out at a frequency of 15 Hz. Each sample of the flow field was generated through an adaptive cross-correlation from the images obtained from two consecutive laser pulses separated by 3 ms in time. For the case of highest reduced velocity analysed ($U^* = 15$), the mean flow velocity was $0.38\ \text{m s}^{-1}$. Thus, a particle would travel around 1 mm between two consecutive laser pulses (which is much less than the characteristic length of the problem, $D = 25\ \text{mm}$). Each PIV area was divided into smaller sub-interrogation areas of 128 pixels \times 128 pixels and, through a parallel self-consistent recomputation of the flow field in successive interrogation areas of 64 pixels \times 64 pixels and 32 pixels \times 32 pixels (or 4.5 mm \times 4.5 mm), with 50% overlap, spatial resolution refinement was obtained (final computations were consistent with the flow fields obtained for larger windows). The final spatial resolution of the flow field for the experimental tests was of the order of 2 mm, which is considered to be sufficient to obtain information of the near-wake vortex shedding structures.

With regard to time resolution, large-scale vortices have a characteristic time scale (related to the Strouhal number, $St = f_v D/U$) of 1–3 Hz for the range of reduced velocities under consideration, which is roughly 5–15 times lower than the acquisition time scale (15 Hz). The recording sequence consisted of 300 frames (lasting 20 s), which is equivalent to approximately 20 oscillation cycles of the circular cylinder. The measurement process was repeated three times for each set of parameters investigated.

2.4. Validation test

To validate the experimental set-up and to obtain reference data for comparison, a non-rotating VIV circular cylinder curve was obtained. As said before, the circular cylinder had a diameter of $D = 25\ \text{mm}$ and submerged length of $L = 430\ \text{mm}$ (aspect ratio $L/D = 17.2$ and blockage ratio of 2.7%). From the mechanical point of view, the mass ratio was $m^* = 11.7$ and damping $\zeta = 0.0043$ (yielding a mass-damping parameter value of $m^*\zeta = 0.0506$). The Re at the peak of the amplitude curve response was $Re = 3200$.

Figure 3 shows the measured VIV response in terms of A^* (A_{10}^*) as a function of the reduced velocity U^* . All measurements have been made with increasing water speed. For comparison purposes, results from Khalak & Williamson (1999), Assi *et al.* (2006) and Klamó (2007) are also given. The mass ratios of Khalak & Williamson (1999) ($m^* = 10.1$), Assi *et al.* (2006) ($m^* = 8.1$) and Klamó (2007) ($m^* = 6.5$) are comparable to our final set-up ($m^* = 11.7$), while the mass-damping parameters were $m^*\zeta = 0.017$, 0.016 and 0.01, respectively, which are smaller than the mass-damping ratio of the present study ($m^*\zeta = 0.0506$). The Reynolds-number ranges of all cases are similar. In particular, the Reynolds number at the amplitude's curve peak was $Re \approx 5000$ for

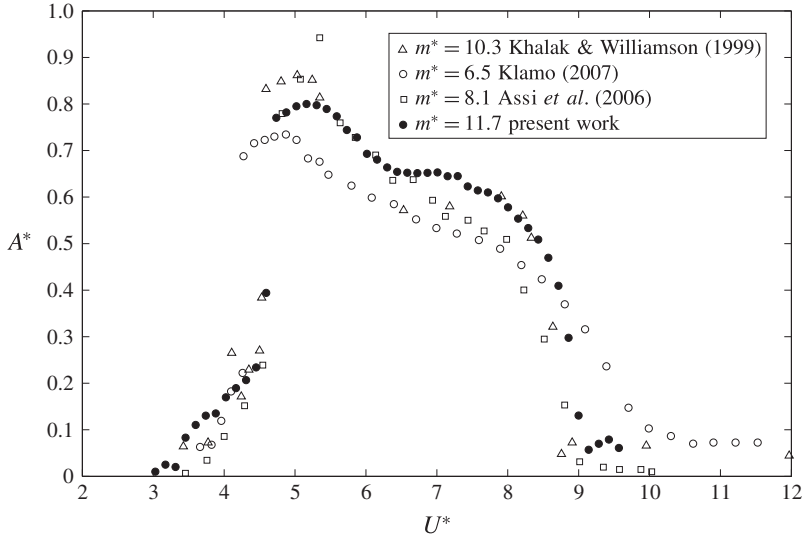


FIGURE 3. Comparison of experimental results for the normalized amplitude variation with reduced velocity. Triangles are from Khalak & Williamson (1999) ($m^* = 10.3$, $\zeta = 0.0017$), open circles are from Klamó (2007) ($m^* = 6.5$, $\zeta = 0.0015$), squares are from Assi *et al.* (2006) ($m^* = 8.1$, $\zeta = 0.0020$) and solid circles stand for the present results ($m^* = 11.7$, $\zeta = 0.0043$).

Khalak & Williamson (1999), $Re \approx 5500$ in Assi *et al.* (2006), $Re \approx 2600$ in Klamó (2007), and $Re \approx 3200$ for the present VIV test.

As can be seen, all VIV responses present three distinctive branches, which correspond to the initial, upper and lower branch, respectively. As described by Govardhan & Williamson (2006), the VIV curve shows three such distinctive branches for high enough Reynolds number and low enough mass-damping parameter. The transition between the initial and upper branches happens at $U^* \approx 4.5$ and a distinctive lower branch can be observed between $U^* \approx 6$ and $U^* \approx 9$ where desynchronization occurs. With respect to the maximum amplitude obtained, the differences appear to be mainly due to the effect of the Reynolds number. This point was studied in Govardhan & Williamson (2006) where a ‘modified Griffin plot’ was introduced and a best fit for a wide range of mass damping and Reynolds number was given as $A_{fit}^* = [1 - 1.12m^*\zeta + 0.3(m^*\zeta)^2] \log_{10}(0.41Re^{0.36})$, which for our experimental set-up yields a theoretical maximum amplitude of oscillation of $A_{fit}^* = 0.82$, which agrees closely with the maximum amplitude measured of $A^* = 0.8$.

With regard to the end conditions, no attached end-plate was used (the effects of end conditions are reviewed in Morse, Govardhan & Williamson (2008)), which leads to a less distinctive upper/lower transition (similar to those from Assi *et al.* (2006) and Klamó (2007)). The decision not to use an end-plate was meant to avoid undesired effects when rotating the cylinder because small misalignments might lead to large damping effects when the cylinder rotates.

The overall agreement is good. As can be seen, all VIV amplitude responses present slight differences, which can be reasonably ascribed to the different experimental conditions listed previously. Other important factors that alter the VIV response, and could explain some differences, include the inflow properties such as its turbulence or uniformity.

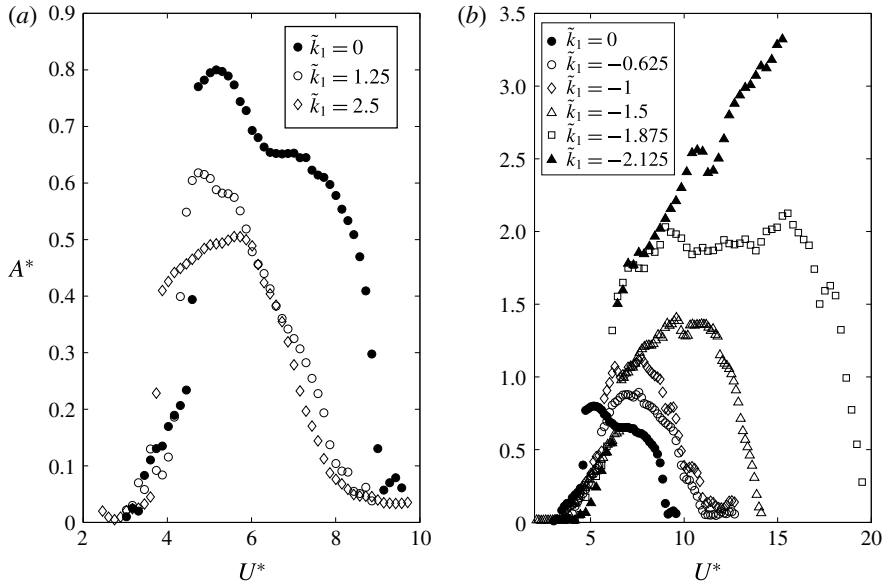


FIGURE 4. Maximum non-dimensional amplitude oscillation as a function of the reduced velocity for (a) positive values and (b) negative values of the rotating parameter \tilde{k}_1 .

3. Results

The effects of rotating the cylinder on its dynamical behaviour (namely the amplitude and frequency of oscillation) are presented here. Two strategies are proposed and compared, focusing mainly on the enhancement in oscillation amplitude or reduction in the oscillations. To better understand the mechanisms underlying the oscillations of the cylinder, PIV visualizations of the near wake are also presented.

3.1. Rotation proportional to position

Firstly, the effect of rotating the cylinder along its axis proportionally to the position of the cylinder will be studied,

$$\theta = \tilde{k}_1 Y, \tag{3.1}$$

where \tilde{k}_1 is a non-dimensional feedback constant that relates the position of the cylinder to the rotation angle of the cylinder along its axis. The cylinder’s response is presented in § 3.1.1 and the different wake patterns in certain configurations are examined in § 3.1.2. A quasi-steady model is developed and presented in § 3.1.3.

3.1.1. Cylinder dynamics

Owing to the character of the rotation imposed, symmetry is not broken and oscillations take place around the equilibrium position without flow ($Y = 0$) for all values of U^* and \tilde{k}_1 . Thus, the cylinder’s response can be described by its main frequency of oscillation $f^* = f/f_N$ and the dimensionless amplitude $A^* = A_{10}/D$ of the cylinder’s steady-state oscillations.

Figure 4 shows the variation of the amplitude of oscillation for different values of \tilde{k}_1 . With respect to the non-rotating case (that is, $\tilde{k}_1 = 0$), positive values of \tilde{k}_1 lead to a reduction of the maximum amplitude of oscillation as well as a reduction of the

region of U^* where the cylinder undergoes large-amplitude oscillations. However, as can be seen, between $\tilde{k}_1 = 1.25$ and $\tilde{k}_1 = 2.5$, the reduction in amplitude of oscillation is not very significant (figure 4b). If \tilde{k}_1 is further increased, the picture does not vary much (regarding amplitude of oscillation, or synchronization region). With respect to the different branches of the curve, transition between the initial and upper branches is anticipated as \tilde{k}_1 increases. Finally, it can be noted that the differentiation between upper and lower branches is increasingly lost.

For negative values of \tilde{k}_1 , the picture is quite different (see figure 4b): oscillations are significantly enhanced and two different responses can be observed. For $-1.8 < \tilde{k}_1 < 0$, the response amplitude exhibits in all cases a bell-shaped evolution as a function of the reduced velocity, which resembles the classical VIV response. This suggests that the vibrations occur under a wake-body synchronization mechanism. As \tilde{k}_1 becomes more negative, oscillations are more intense, the range of synchronization is enlarged, and the reduced velocity at which maximum amplitude is achieved is delayed as well as the initial-upper branch transition. A different behaviour has been found when $\tilde{k}_1 < -1.8$. As can be observed, for $\tilde{k}_1 = -2.125$, just after the initial-lower transition, A^* seems to adopt a quasi-linear dependence on the reduced velocity. This resembles the dependence of galloping-type instability where motion-induced forces are dominant, in contrast to VIV where fluid forces are mainly driven by vortex shedding. For $\tilde{k}_1 = -2.125$, values up to $U^* = 16$ only are presented. The reason has to do with the actual limitations of the experimental set-up. Specifically, beyond that threshold, the amplitude of the oscillations of the elastic blades is such that their elastic response starts to lose linearity. This raises the question of whether a galloping-like response will continue forever, or at some value of the reduced velocity the oscillations would start to decay. To analyse this point in more detail, an analysis of the near-wake flow pattern is made in the following subsection (figure 7), which shows that synchronization between vortex shedding and oscillations is lost. In addition, a quasi-steady model is developed in the next section, which explains the galloping-type response observed. The value $\tilde{k}_1 = -1.875$ shows an intermediate behaviour: after the initial-upper branch transition, the amplitude response curve adopts a linear trend with the reduced velocity, but at $U^* \approx 10$ it loses this trend following an almost constant amplitude of oscillation for increasing U^* until large-amplitude oscillations cease abruptly at $U^* = 20$.

In figure 5, the normalized frequency of oscillations f^* is plotted as a function of the reduced velocity for different values of \tilde{k}_1 . Owing to the large value of the reduced mass, variation of f^* with U^* is relatively small. In the initial branch the frequency is lowered slightly and then increases linearly with U^* . For $\tilde{k}_1 > 0$ the slope of the frequency variation with U^* is significantly increased. On the other hand, for negative values of \tilde{k}_1 (up to $\tilde{k}_1 > -1.8$), f^* is lowered and the slope with U^* is smaller. Importantly, for large negative values of \tilde{k}_1 (i.e. $\tilde{k}_1 < -1.8$), f^* reaches a near-constant value after $U^* \approx 10$. This result reinforces the idea that for large negative values of \tilde{k}_1 the cylinder undergoes galloping-type oscillations. Seemingly, the initial-upper branch transition occurs near $f^* = 1$ for all values of \tilde{k}_1 (similar to the classical VIV response).

3.1.2. PIV of the near wake for rotation proportional to the position

Here, PIV visualizations of the near wake are presented to understand the effect of the rotation of the cylinder on the wake patterns. Non-dimensional vorticity contours are given for different values of \tilde{k}_1 at two values of the reduced velocity, $U^* = 5.2$

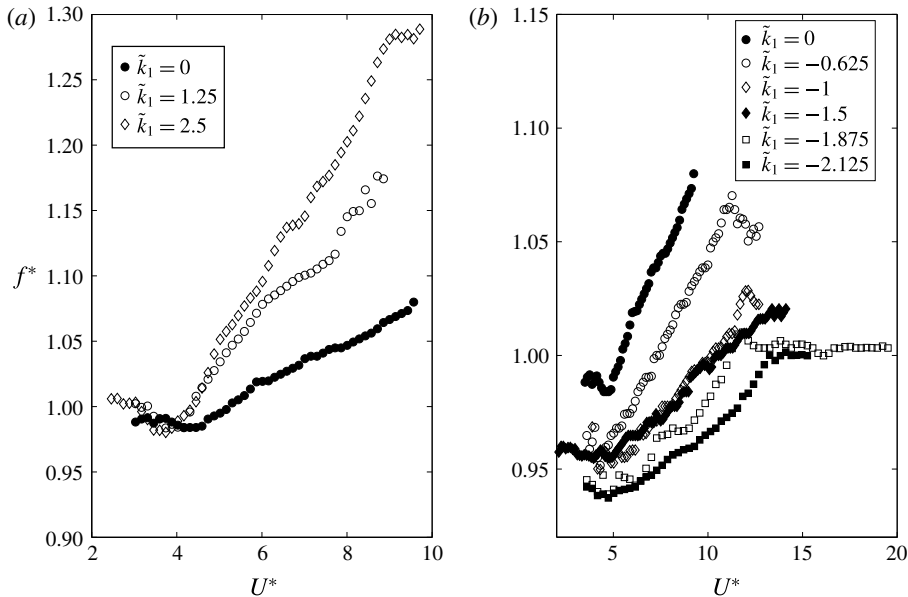


FIGURE 5. Non-dimensional oscillating frequency of the cylinder as a function of the reduced velocity for (a) positive values and (b) negative values of the rotating parameter \tilde{k}_1 .

(near the peak amplitude) and $U^* = 7.5$, which correspond to the upper and lower branches, respectively, in the classical VIV curve ($\tilde{k}_1 = 0$). The non-dimensional vorticity contour images have been treated by proper orthogonal decomposition (POD) so as to retain high-level energy modes and to filter high spatial and temporal frequencies (for further details, the reader is referred to Berkooz, Holmes & Lumley (1993) and Ma *et al.* (2003)).

As mentioned earlier, the classical VIV response, for the Reynolds numbers under consideration ($Re = 3200$) and for low enough mass-damping parameter ($m^*\zeta = 0.0506$), is characterized by a three-branch curve. Regarding the wake patterns, the initial branch is characterized by a 2S mode of vortex emission at the centreline. The upper branch presents a $2P_0$ mode of vortex shedding structure (as described in Morse & Williamson (2009)), which consists of two pairs of vortices shed per cycle where the secondary vortex has a intensity of circulation smaller than the main vortex (figure 6a). In the lower branch, the secondary vortex has grown in intensity developing into a full 2P mode (figure 6b). Further increasing the velocity leads to a desynchronization between vortex emission and oscillation.

For $\tilde{k}_1 > 0$, the wake structure in the initial branch is equivalent to the case without actuation (2S vortices shed near the centreline). After the transition, near the peak amplitude, the secondary vortex is reduced and even disappears as \tilde{k}_1 grows (figure 6c), thus evolving from a $2P_0$ mode to a 2S mode of vortex shedding (as \tilde{k}_1 is increased) where two single vortices are shed per cycle at the outer part of the oscillation's cycle (near its maximum amplitude). Also, the main vortex reduces its intensity compared to the case without actuation. This phenomenon probably occurs because the cylinder rotates in the opposite direction to the vortex being shed, therefore reducing the intensity of the circulation of the vortex shed, which contributes to a reduction of the amplitude of oscillation. As will be seen in the next

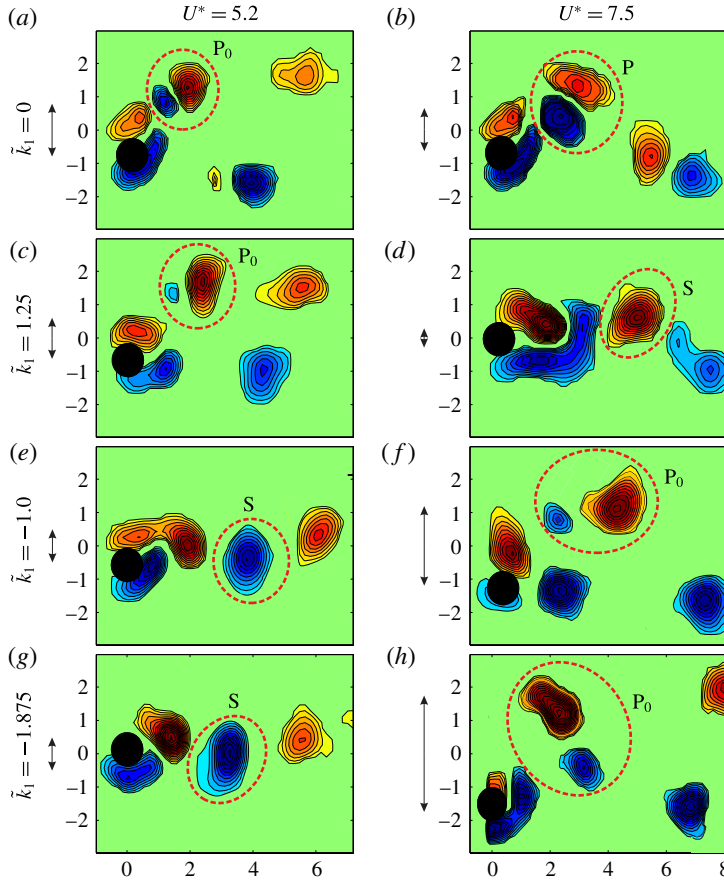


FIGURE 6. (Colour online) Non-dimensional vorticity contours $\omega D/U$ for two values of reduced velocity ($U^* = 5.2, 7.5$) and four values of \tilde{k}_1 ($\tilde{k}_1 = 0, 1.25, -1.0, -1.875$), respectively. Red indicates clockwise circulation and blue indicates anticlockwise circulation. Vortical structures are highlighted with a red dashed line. P represents a pair of vortices shed per half-cycle corresponding to a 2P mode of vortex shedding. P_0 is equivalent to the previous one but with the secondary vortex being qualitatively smaller (circulation intensity-wise). S structures represent a single vortex being shed per half-cycle, which corresponds to a 2S mode of vortex shedding. Note that, for completeness, the amplitude of oscillation for each case is indicated by a double-headed arrow.

subsection (§3.1.3), from a quasi-steady point of view, the lift coefficient depends on the rate of rotation, and positive values of \tilde{k}_1 lead to a lift coefficient opposite to the velocity of displacement, thus contributing to a reduction of the amplitude of oscillation expected. Finally, as U^* grows, the upper and lower branches are no longer distinguishable and desynchronization is anticipated (figure 6d).

For $\tilde{k}_1 < 0$, the transition between the initial and upper branch is delayed; thus figure 6(e,g) shows a 2S vortex emission mode at the centreline, as these contours still represent the wake structure of the initial branch. As U^* increases, after the transition, a $2P_0$ mode is obtained (or 2P mode). The vortices shed increase in strength (compared to $\tilde{k}_1 = 0$) as \tilde{k}_1 becomes more negative, because the rotation of the cylinder is in the same direction as that of the vortices being shed, thus increasing

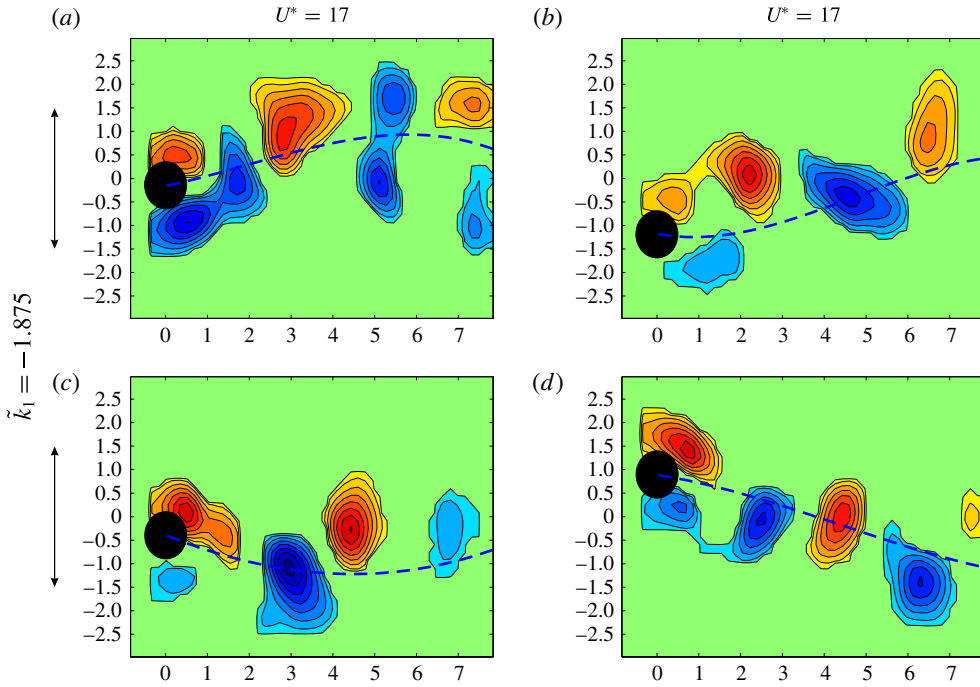


FIGURE 7. (Colour online) Non-dimensional vorticity $\omega D/U$ contours for $U^* = 17$ and $\tilde{k}_1 = -1.875$ evaluated at four different displacements of the cylinder. Red indicates clockwise circulation and blue indicates anticlockwise circulation. The amplitude of oscillation is indicated by the double-headed arrow.

the circulation of such vortices (figure 6*f,h*). The vorticity flux from the surface of the cylinder to the flow is $\Gamma_s = -\pi D u_w$, where u_w is the circumferential cylinder speed. For this rotating law, $u_w = D k_1 \dot{y} / 2$ and therefore $\Gamma_s = -\pi D^2 k_1 \dot{y} / 2$, which suggests that vorticity emission from the cylinder’s surface contributes to increasing the circulation of the shed vortex when k_1 is negative. This contributes to the enhancement of the amplitude of oscillation. Noticeably, the vortices are shed at the outer part of the oscillation’s cycle; thus, it seems that the rotation of the cylinder (for the range of \tilde{k}_1 investigated) does not modify the phase at which such vortical structures are emitted.

The increase in amplitude is also related to the lift coefficient that appears due to the rotation of the cylinder (from a quasi-steady point of view) in the direction of the velocity of displacement, thus contributing to the enhancement of the oscillations for negative values of \tilde{k}_1 .

Furthermore, a case for $U^* = 17$ and $\tilde{k}_1 = -1.875$ is analysed to observe the mechanism underlying oscillations for large negative values of \tilde{k}_1 and large U^* . In figure 7, four different time snapshots are presented, and overprinted in a blue dashed line is the past trajectory of the cylinder. As can be observed, the picture is very different from the previous ones where there was synchronization between vortex emission and oscillation of the cylinder. In this case, the vortices are shed independently of the cylinder’s oscillation at its own frequency and thus the wake pattern resembles that of a wave as each vortex is shed independently at different points of the cycle of oscillation. In particular, the normalized vortex emission frequency is $f_v^* = f_v / f_N = 3.44$, which compares reasonably well to that of the Strouhal

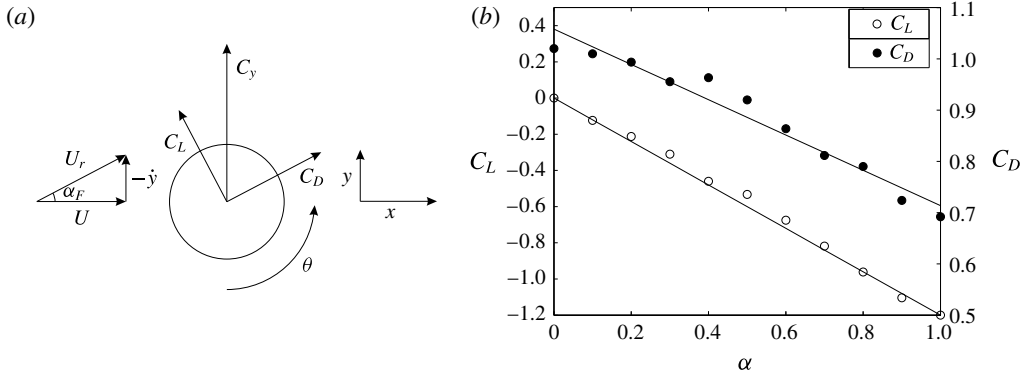


FIGURE 8. (a) Schematics of the forces acting on the cylinder in a quasi-steady situation. (b) Average transverse force coefficient and average in-line force coefficient as a function of the dimensionless rotation rate α . Experiments to determine C_L and C_D have been carried out at $Re \approx 9000$, which corresponds to $U^* = 15$ for the current set-up. Dashed lines represent the linear best fits.

value of vortex emission for a cylinder at rest ($St = 0.21$), which yields $f_{vrest}^* = 3.57$ ($= StU^*$). Thus, for large values of negative \tilde{k}_1 and reduced velocity, there is no synchronization between vortex emission and oscillation, and the amplitude response tends to a linear dependence with U^* resembling a galloping-type oscillation.

3.1.3. *Quasi-steady model for galloping-type response*

As observed in the previous subsection, there is a clear separation in the dynamical behaviour between the cases for $\tilde{k}_1 > -1.8$ and those where $\tilde{k}_1 < -1.8$. In the latter case, from a certain value of the reduced velocity, the amplitude of oscillation increases linearly with the reduced velocity, leading one to assume that some kind of galloping-type phenomenon is happening. Also, the frequency of vortex emission for large U^* follows the Strouhal law, therefore increasing linearly with U^* , whereas the frequency of oscillation is locked at $f^* \approx 1$. A quasi-steady model is proposed here to explain the observed behaviour, to determine for which values of \tilde{k}_1 a galloping-type behaviour is expected to hold, and to see the capability of the model to predict the cylinder’s dynamics by comparing the amplitude of oscillation given by the quasi-steady model with experimental results.

For the quasi-steady analysis, it is assumed that the instantaneous transverse force can be obtained from the steady lift and drag force with an equivalent instantaneous velocity and angle of attack α_F (Blevins 1990). In figure 8(a) a scheme of the equivalent configuration is shown.

Taking into account the lift and drag force coefficients and projecting onto the transverse (cross-flow) direction, one has

$$C_y = \frac{U_r}{U} (-C_L \cos(\alpha_F) - C_D \sin(\alpha_F)) = -\frac{C_L}{\cos(\alpha_F)} - C_D \frac{\tan(\alpha_F)}{\cos(\alpha_F)}, \quad (3.2)$$

where α_F is the instantaneous angle of attack, $\tan(\alpha_F) = -\dot{y}/U$, $\cos(\alpha_F) = U/U_r$, U_r is the relative incident flow speed ($U_r = \sqrt{U^2 + \dot{y}^2}$), and C_L and C_D are, respectively, the lift and drag time-averaged fluid force coefficients, which can be obtained from

the ‘static’ configuration as a function of the dimensionless rotation rate. Figure 8(b) shows the lift and drag coefficient variations with the dimensionless rotation rate obtained from experiments carried out in a water channel where the rotation rate was fixed at different values and fluid forces were measured using a force sensor. Assuming, as a first approximation, a linear variation with the rotation rate of C_L and C_D , one has

$$C_L = C_{L\alpha}\alpha = C_{L\alpha}\frac{\dot{\theta}D}{2U_r}, \tag{3.3a}$$

$$C_D = C_{D0} - C_{D\alpha}|\alpha| = C_{D0} - C_{D\alpha}\left|\frac{\dot{\theta}D}{2U_r}\right|. \tag{3.3b}$$

When the cylinder rotates proportionally to the cylinder’s displacement ($\theta' = \tilde{k}_1 Y'$), (3.3a) and (3.3b) can be written in dimensionless form as

$$C_L = \frac{C_{L\alpha}}{2}\tilde{k}_1\frac{Y'}{U_r^*}, \tag{3.4a}$$

$$C_D = C_{D0} - \frac{C_{D\alpha}}{2}\left|\tilde{k}_1\frac{Y'}{U_r^*}\right|, \tag{3.4b}$$

where $U_r^* = U_r/f_N D = U^*/\cos(\alpha_F)$ is the non-dimensional relative incident flow velocity. From figure 8(b), the linear best fit yields $C_{L\alpha} = -1.2$, $C_{D0} = 1.06$ and $C_{D\alpha} = 0.36$, which are in good agreement when compared to similar experiments and numerical simulations (Mittal & Kumar 2003; Karabelas *et al.* 2012; Bourguet & Jacono 2014). Introducing (3.4a) and (3.4b) into (3.2), and taking into account that $\cos(\alpha_F)^{-1} = U_r/U$, one obtains

$$C_y = -\frac{C_{L\alpha}}{2}\tilde{k}_1\frac{Y'}{U^*} - C_{D0}\frac{Y'}{U^*}\sqrt{1 + \left(\frac{Y'}{U^*}\right)^2} + \frac{C_{D\alpha}}{2}\left|\tilde{k}_1\frac{Y'}{U^*}\right|\frac{Y'}{U^*}, \tag{3.5}$$

which is the transverse fluid force coefficient evaluated from a quasi-steady basis. This model for the transverse force coefficient mainly neglects the effect of the vortices shed (note that there is no fluid force without cylinder motion), which is theoretically valid for U^* large enough with respect to St^{-1} (Parkinson 1989). The first term in (3.5) can be seen as a positive linear damping for $\tilde{k}_1 > 0$, reducing possible amplitude oscillations, or as a linear negative damping term for $\tilde{k}_1 < 0$, which, on the other hand, contributes to amplifying the amplitude of oscillations. The last two terms are nonlinear damping terms associated with the drag force. Note that there is no stiffness term that could significantly change the frequency of oscillation, thus leading to the result that the frequency of oscillation should coincide with f_N , that is, $f^* = 1$ (which agrees well with results shown in figure 5(b) for $\tilde{k}_1 = -1.875$ and $\tilde{k}_1 = -2.125$ for large reduced velocities).

It is of interest to study the theoretical value of \tilde{k}_1 from which the galloping-type response is expected to occur according to the quasi-steady model. To do so, note that (3.5) can be linearized retaining only the linear terms:

$$C_y \approx -\frac{C_{L\alpha}}{2}\tilde{k}_1\frac{Y'}{U^*} - C_{D0}\frac{Y'}{U^*}. \tag{3.6}$$

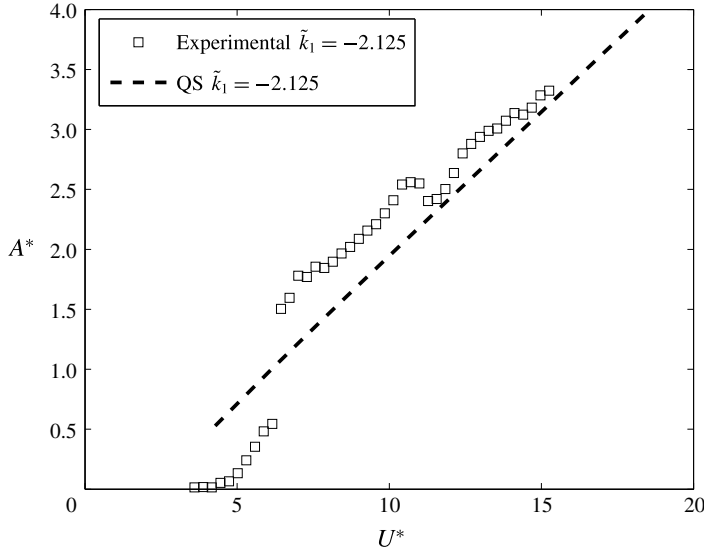


FIGURE 9. Comparison between quasi-steady solution and the present experimental results for $\tilde{k}_1 = -2.125$.

Galloping-type oscillations may occur when the linearized term of the transverse force coefficients yields a positive value only, thus

$$\tilde{k}_1 < -\frac{2C_{D\alpha}}{C_{L\alpha}} \simeq -1.76, \tag{3.7}$$

which compares well with the results found during experimental results, since galloping-type oscillations appeared for $\tilde{k}_1 < -1.8$. To obtain the amplitude of oscillations, the dynamical equation for the cylinder (2.2a) along with C_y given by (3.5) can be solved analytically by the harmonic balance method such as in Vicente-Ludlam *et al.* (2014) and Vicente-Ludlam, Barrero-Gil & Velazquez (2015, 2017) or numerically with a Runge–Kutta scheme.

Figure 9 assesses the validity of the quasi-steady model proposed with the present experimental results for $\tilde{k}_1 = -2.125$ with good agreement for high enough reduced velocity (say $U^* > 8$) with errors smaller than 10%. This reinforces the idea that for large negative values of \tilde{k}_1 and enough reduced velocities the cylinder is driven mainly for motion-induced fluid forces, which can be reasonably well described by the quasi-steady hypothesis. However, for $\tilde{k}_1 = -1.875$ the quasi-steady model fails to predict the amplitude of oscillations of the experimental data since, after an initial linear trend with U^* , the amplitude of oscillations keeps a nearly constant value until these cease at $U^* = 20$. This could be caused by the low value of the linear part of the transverse force from (3.5) at this value of \tilde{k}_1 , which is very close to the minimum theoretically predicted by the quasi-steady model, making other phenomena not taken into account in the quasi-steady model overcome the galloping-type oscillations.

3.2. Rotation proportional to the cylinder’s velocity ($\theta = \tilde{k}_2 Y'$)

Another strategy that has been studied is to modify the response of a circular cylinder undergoing VIV by rotating the cylinder proportionally to its own transverse velocity.

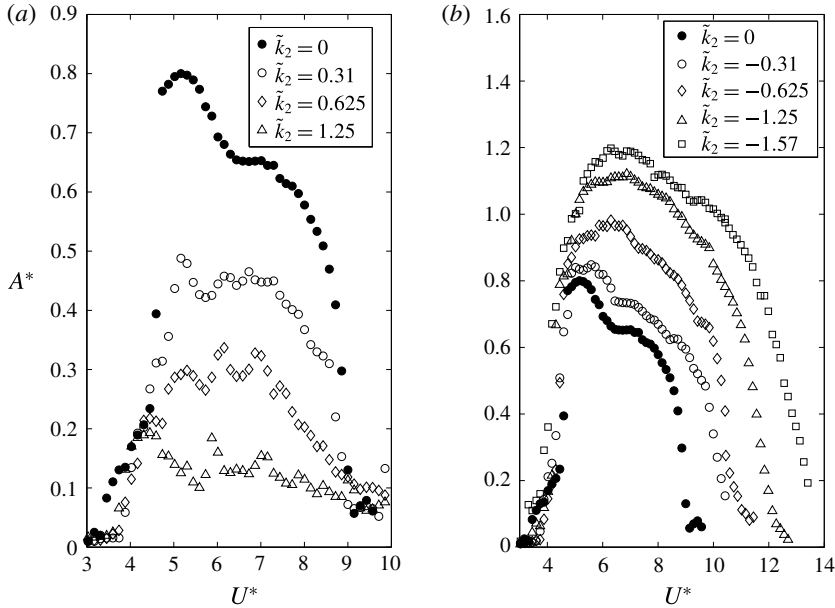


FIGURE 10. Maximum non-dimensional amplitude oscillation as a function of the reduced velocity for (a) positive values and (b) negative values of the rotating parameter \tilde{k}_2 .

Results including amplitude and frequency of oscillation and non-dimensional vorticity contours are presented here. In what follows, the cylinder is rotated according to the feedback equation

$$\theta = \tilde{k}_2 Y', \tag{3.8}$$

where \tilde{k}_2 is a non-dimensional feedback constant. The cylinder’s response is presented in § 3.2.1 and the different wake patterns in certain configurations are examined in § 3.2.2.

3.2.1. Cylinder dynamics

In figure 10, the amplitude of oscillation of the cylinder is plotted as a function of the reduced velocity for different values of \tilde{k}_2 . For $\tilde{k}_2 > 0$ the response is greatly attenuated with respect to the curve without actuation (figure 10a, see curve $\tilde{k}_2 = 0$). With $\tilde{k}_2 = 1.25$, the peak amplitude is $A^* \approx 0.22$ whereas when rotating proportionally to the cylinder’s displacement, for $\tilde{k}_1 = 2.5$ (which approximately leads to twice the level of rotation for a prescribed amplitude of oscillation) the maximum oscillation does not exceed $A^* = 0.5$ (as was shown in figure 4a). Thus rotating the cylinder proportionally to its velocity of oscillation is considerably more efficient in terms of attenuating the amplitude of oscillation with less actuation. On the other hand, negative values of \tilde{k}_2 lead to an increase of the amplitude of oscillation as well as an increase of the synchronization region undergoing large-amplitude oscillations. However, as can be seen in figure 10(b), further decreasing \tilde{k}_2 does not modify the type of response obtained, namely, no galloping-type oscillations have been found. This result can be explained through the quasi-steady model, which gives the

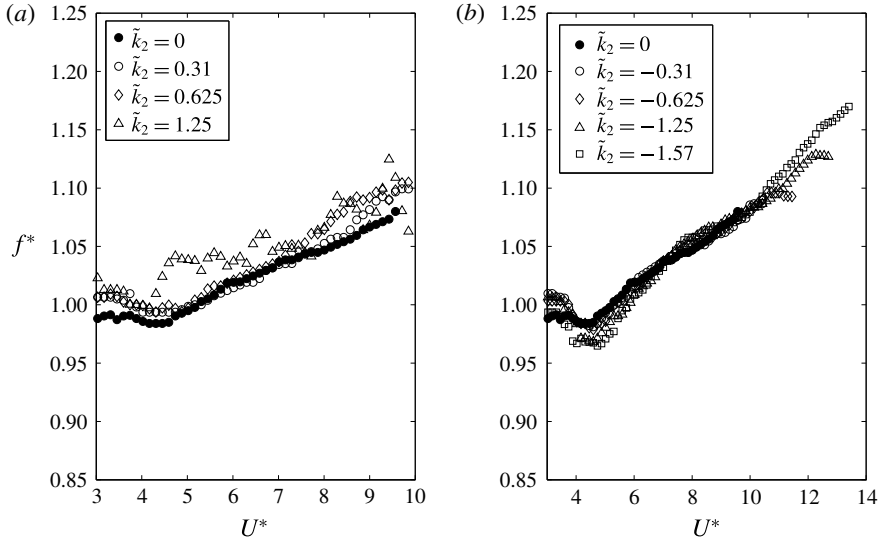


FIGURE 11. Non-dimensional oscillating frequency of the cylinder as a function of the reduced velocity for (a) positive values and (b) negative values of the rotating parameter \tilde{k}_2 .

following transverse fluid force coefficient:

$$C_y = -\frac{C_{L\alpha}}{2} \tilde{k}_2 \frac{Y''}{U^*} - C_{D\alpha} \frac{Y'}{U^*} \sqrt{1 + \left(\frac{Y'}{U^*}\right)^2} + \frac{C_{D\alpha}}{2} \left| \tilde{k}_2 \frac{Y''}{U^*} \right| \frac{Y'}{U^*}. \quad (3.9)$$

This equation is obtained in the same way as (3.5), but taking into account that rotation is now proportional to the velocity of oscillation. From (3.9) note that it is not possible to introduce negative damping that can overcome the damping introduced by the drag coefficient. Thus, the increase of the amplitude of oscillations has to be explained by the modification of the structure of the near wake (namely, intensity of vortices shed). The transition between the initial and upper branch is not as pronounced as it is for the case without actuation (or when rotating the cylinder proportionally to its position), and the reduced velocity at which the transition occurs is not modified by \tilde{k}_2 . Also, the distinction between the upper and lower branches is lost as actuation (either positive or negative) is increased.

Finally, with regard to the frequency of oscillation (figure 11), \tilde{k}_2 does not modify f^* significantly. The value of the non-dimensional frequency of oscillation nearly fits into a single curve for all values of \tilde{k}_2 , thus explaining why the initial–upper branch transition occurs at similar reduced velocity as the frequency of oscillation reaches $f^* = 1$ at nearly the same reduced velocity. Negative values of \tilde{k}_2 (figure 11b) increase the region of synchronization; therefore, the frequency of oscillation keeps growing with the same slope until desynchronization occurs (for larger U^* as \tilde{k}_2 becomes more negative).

3.2.2. PIV of the near wake for rotation proportional to the velocity of displacement

For positive values of \tilde{k}_2 , the initial branch is not modified with respect to the case without actuation (presenting a 2S mode of vortex shedding at the centreline).

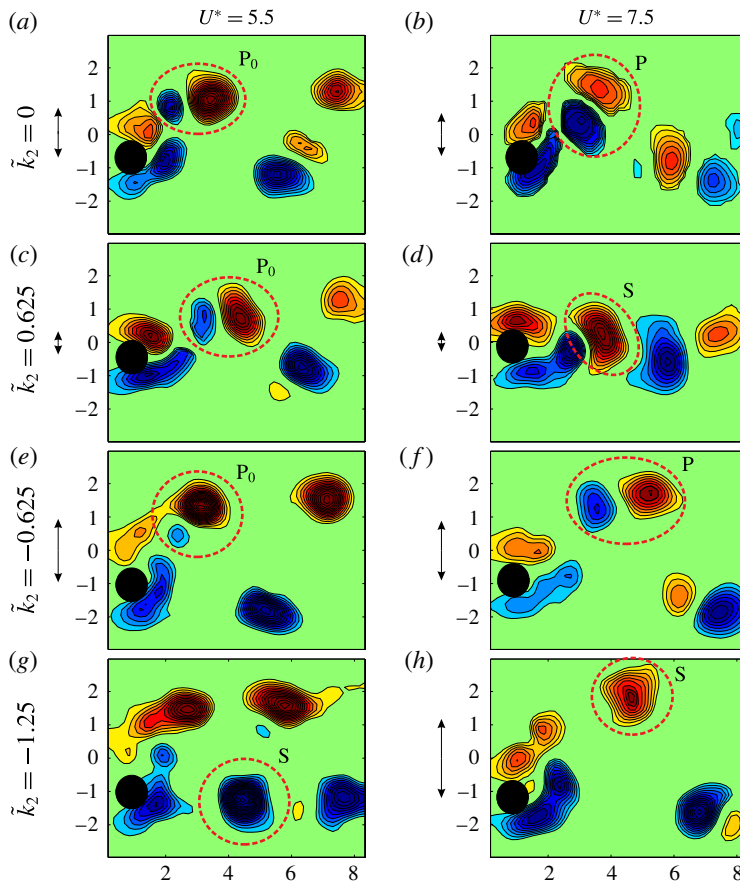


FIGURE 12. (Colour online) Non-dimensional vorticity contours for two values of reduced velocity ($U^* = 5.5, 7.5$) and four values of \tilde{k}_2 ($\tilde{k}_2 = 0, 0.625, -0.625, -1.25$), respectively. Red indicates clockwise circulation and blue indicates anticlockwise circulation. Vortical structures are highlighted with a red dashed line. P represents a pair of vortices shed per half-cycle corresponding to a 2P mode of vortex shedding. P_0 is equivalent to the previous one but with the secondary vortex being qualitatively smaller (circulation intensity-wise). S structures represent a single vortex being shed per half-cycle, which corresponds to a 2S mode of vortex shedding. Note that, for completeness, the amplitude of oscillation for each case is indicated by a double-headed arrow.

At $U^* = 5.5$ for $\tilde{k}_2 = 0$ (which corresponds to the upper branch), a $2P_0$ mode of vortex shedding was observed (figure 12a). As \tilde{k}_2 increases, the amplitude of oscillation diminishes and still a $2P_0$ mode is observable (figure 12c, $\tilde{k}_2 = 0.625$), though circulation intensity is reduced and vortices are shed nearer to the centreline. Further raising of \tilde{k}_2 leads to an increasingly undefined wake pattern where $2P$ vortex emission is mixed with $2S$ mode alternately (driven by the low amplitude of oscillation as well as the rotation of the cylinder). As the reduced velocity is increased ($U^* = 7.5$), the picture is similar where $2P$ vortex emission (for $\tilde{k}_2 = 0$, figure 12b) slowly evolves to a $2S$ mode as \tilde{k}_2 increases (figure 12d exhibits a fully $2S$ mode for $\tilde{k}_2 = 0.625$ and amplitude of oscillation lower than 0.2).

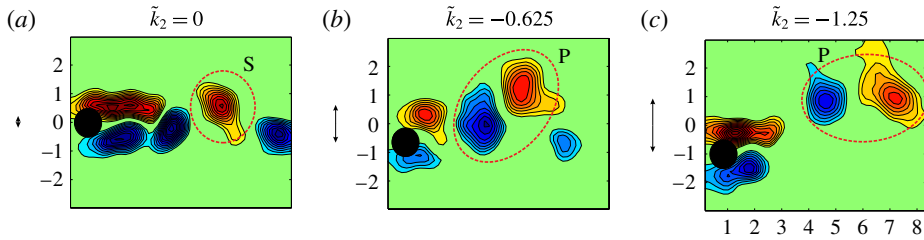


FIGURE 13. (Colour online) Non-dimensional vorticity contours for $U^* = 9.5$ and three values of \tilde{k}_2 ($\tilde{k}_2 = 0, -0.625, -1.25$), respectively. Red indicates clockwise circulation and blue indicates anticlockwise circulation. Vortical structures are highlighted with a red dashed line. P represents a pair of vortices shed per half-cycle corresponding to a 2P mode of vortex shedding. P₀ is equivalent to the previous one but with the secondary vortex being qualitatively smaller (circulation intensity-wise). S structures represent a single vortex being shed per half-cycle, which corresponds to a 2S mode of vortex shedding. Note that, for completeness, the amplitude of oscillation for each case is indicated by a double-headed arrow.

For negative \tilde{k}_2 , the initial branch is not modified (2S mode). After the transition, in the upper branch ($U^* = 5.5$), negative \tilde{k}_2 markedly increases the circulation of the vortices shed compared to the case without actuation, and the secondary vortex is suppressed as \tilde{k}_2 is diminished (figure 12*e,g*). For $U^* = 7.5$ a 2P mode of vortex emission (similar to $\tilde{k}_2 = 0$) is obtained with increasing vortex circulation intensity as \tilde{k}_2 is diminished with also a diminishing intensity of the secondary vortex (figure 12*f,h*). As observed, rotating the cylinder proportionally to its velocity mainly affects the intensity of the vortices shed for this range of U^* without affecting the phase of vortex emission. For this rotating law, the vorticity flux from the surface of the cylinder is $\Gamma_s = -\pi D^2 k_2 \ddot{y} / 2$ (note that circumferential velocity at the cylinder's surface is $Dk_2 \dot{y} / 2$). This suggests that more circulation in the shed vortex is expected for negative values of k_2 . Observe that if we consider $\ddot{y} \approx -2\pi f^2 y$ (since oscillations have a harmonic character), it follows that Γ_s is in phase with the cylinder's displacement. This may help to accommodate vorticity generation in the surface onto the growing vortex, increasing its circulation significantly.

Notably, as seen in figure 10(*b*), the synchronization region can be enlarged with negative \tilde{k}_2 . In particular, non-dimensional vorticity contour maps are given at $U^* = 9.5$ for the case without actuation ($\tilde{k}_2 = 0$, figure 13*a*) and two negative values of \tilde{k}_2 ($\tilde{k}_2 = -0.625, \tilde{k}_2 = -1.25$, figures 13*b* and 13*c*, respectively). As observed, for $\tilde{k}_2 = 0$, oscillations are small due to desynchronization between vortex emission and the cylinder's oscillation. However, as \tilde{k}_2 becomes more negative, the synchronization region is enlarged and large-amplitude oscillations occur and a fully developed 2P mode can be observed.

Finally, no quasi-steady flow pattern has been found with regard to the wake pattern (as deduced from (3.9)).

4. Concluding remarks

Hydroelastic experiments have been performed to study the dynamical behaviour and wake pattern of the fluid flow around a circular cylinder undergoing FIV ($m^* = 11.7$ and Reynolds number in the range 1500–10 000), free to oscillate in

the transverse direction with an imposed rotation around its axis linked to the cylinder's dynamics. Two different rotating laws have been investigated: first, a rotation proportional to the cylinder's displacement; second, a rotation proportional to the cylinder's velocity. The main findings are as follows.

(i) Regarding the case where rotation is proportional to the cylinder's displacement ($\theta = \tilde{k}_1 Y$), it has been found that positive values of \tilde{k}_1 lead to a reduction in the maximum amplitude of oscillation compared to that of the non-rotating VIV, and the transition between the initial and lower branch happened for lower values of reduced velocities. Also, the frequency of oscillation was slightly increased and the region of VIV synchronization was diminished. On the other hand, negative values of \tilde{k}_1 significantly increase the maximum peak value of oscillations and increase the reduced velocity at which this maximum occurs. Also, the region of synchronization is greatly enlarged as \tilde{k}_1 becomes more negative. In fact, if \tilde{k}_1 overcomes a certain negative value, the response obtained changes dramatically and a galloping-type response is obtained, where the amplitude of oscillation increases almost linearly for high values of the reduced velocity. In those cases, the frequency of oscillation remains constant (f^* close to 1) for high values of reduced velocity and the frequency of vortex shedding increases approximately following the Strouhal law, and thus both time scales (oscillation and vortex shedding) depart from each other. A large number (increasing with the reduced velocity) of vortices are shed per oscillation cycle. From the practical side, note that negative values of \tilde{k}_1 could be of interest for energy harvesting purposes as well as to promote mixing.

(ii) A quasi-steady model has been proposed to predict the amplitude of oscillation for large negative values of \tilde{k}_1 as well as to better understand the observed results. When the time scales of the vortex emission and the oscillation period are insignificantly different, the force can be considered in a quasi-steady fashion and the C_y force coefficient can be expressed as a function of Y'/U^* . Following (3.5), the galloping condition is fulfilled for negative values larger than $\tilde{k}_1 < -2C_{D0}/C_{L\alpha} = -1.76$, which agrees well with the experimental results. The quasi-steady model predicts a linear dependence of the amplitude of oscillation on the reduced velocity. As \tilde{k}_1 becomes more negative, the slope of the amplitude oscillation with the reduced velocity increases. The quasi-steady model was compared to experimental results with good agreement between them.

(iii) For the case where rotation is proportional to the cylinder's velocity ($\theta = \tilde{k}_2 Y'$), it has been found that positive values of \tilde{k}_2 lead to a reduction in the maximum amplitude of oscillation compared to that of the pure VIV. Notably, this rotation law leads to greater reduction of the amplitude of oscillation of the cylinder with less actuation compared to rotating the cylinder proportionally to its displacement (with $\tilde{k}_1 > 0$), so rotation proportional to velocity should be applied to reduce the amplitude of oscillations efficiently. On the other hand, negative values of \tilde{k}_2 increase the maximum value of oscillation. Regarding the frequency of oscillation, it nearly fits into a single curve for all values of \tilde{k}_2 . Negative values of \tilde{k}_2 increase the region of synchronization; thus f^* keeps growing with U^* until desynchronization occurs and the vortex shedding frequency is always synchronized with the frequency of oscillation. For all values of \tilde{k}_2 , oscillations occur under VIV (bell-shaped evolution as a function of the reduced velocity).

(iv) The quasi-steady model developed helps to explain why a galloping-type response is not expected to occur for the case of rotating the cylinder proportional

to its oscillating velocity, since the linear transverse force term associated with the rotation is proportional to the acceleration. Therefore, there is no excitation that overcomes the damping term introduced by the drag force. This agrees with experimental results and PIV visualizations performed in which all large-amplitude oscillations obtained occur under a VIV-type solution.

(v) In general, investigated wake modes found for the parameter set of U^* , \tilde{k}_1 and \tilde{k}_2 are equivalent to those observed for the non-rotating case (Morse & Williamson 2009), that is, modes 2S, 2P₀ and 2P. Rotation of the cylinder mainly modifies the intensity of the circulation of the vortices shed. Positive values of \tilde{k}_1 and \tilde{k}_2 lead to a reduction in their intensity of circulation whereas negative values of \tilde{k}_1 and \tilde{k}_2 increase such intensity as a general trend. This is caused mainly by the direction of rotation of the cylinder as well as its rotation rate. However, for high enough negative values of \tilde{k}_1 and high U^* , a new wake mode of vortex shedding has been found where the vortex formation is decoupled from the oscillation of the cylinder. The vortices are shed independently from the cylinder's oscillation at its own frequency and thus the wake pattern resembles that of a wave, as each vortex is shed at different points of the cycle of oscillation. The shedding frequency of the vortices was found to compare well with the frequency given by the Strouhal law. From the applied side, the ability of the rotation law to fix a certain wake pattern can be of interest for some applications (mixing, heat transport, etc.). Further experiments for higher values of the feedback constants \tilde{k}_1 and \tilde{k}_2 should be performed to determine if new modes of vortex emission emerge.

Acknowledgements

A.V. has been funded by the Spanish Ministry of Economy and Competitiveness (Ministerio de Economía y Competitividad) under research contract DPI2016-75296-P, and gratefully acknowledges this support.

Supplementary movies

Supplementary movies are available at <https://doi.org/10.1017/jfm.2018.332>.

REFERENCES

- ABDELKEFI, A., HAJJ, M. R. & NAYFEH, A. H. 2012 Power harvesting from transverse galloping of square cylinder. *Nonlinear Dyn.* **70** (2), 1355–1363.
- ABDELKEFI, A., HAJJ, M. R. & NAYFEH, A. H. 2013 Piezoelectric energy harvesting from transverse galloping of bluff bodies. *Smart Mater. Struct.* **22** (1), 015014.
- AL-MDALLAL, Q. M. 2004 Analysis and computation of the cross-flow past an oscillating cylinder with two degrees of freedom. PhD thesis, Memorial University of Newfoundland.
- ASSI, G. R. S., MENEGHINI, J. R., ARANHA, J. A. P., BEARMAN, P. W. & CASAPRIMA, E. 2006 Experimental investigation of flow-induced vibration interference between two circular cylinders. *J. Fluids Struct.* **22** (6), 819–827.
- BARRERO-GIL, A., SANZ-ANDRES, A. & ALONSO, G. 2010 Energy harvesting from transverse galloping. *J. Sound Vib.* **329** (14), 2873–2883.
- BARRERO-GIL, A., PINDADO, S. & AVILA, S. 2012 Extracting energy from vortex-induced vibrations: a parametric study. *Appl. Math. Model.* **36** (7), 3153–3160.
- BEARMAN, P. W. 2011 Circular cylinder wakes and vortex-induced vibrations. *J. Fluids Struct.* **27**, 648–658.

- BERKOOZ, G., HOLMES, P. & LUMLEY, J. L. 1993 The proper orthogonal decomposition in the analysis of turbulent flows. *Annu. Rev. Fluid Mech.* **25** (1), 539–575.
- BERNITSAS, M. M., RAGHAVAN, K., BEN-SIMON, Y. & GARCIA, E. M. H. 2008 VIVACE (Vortex Induced Vibration Aquatic Clean Energy): a new concept in generation of clean and renewable energy from fluid. *Trans. ASME J. Offshore Mech. Arctic Engng* **130** (4), 041101.
- BLACKBURN, H. M., ELSTON, J. R. & SHERIDAN, J. 1999 Bluff body propulsion produced by combined rotary and translational oscillation. *Phys. Fluids* **11** (1), 4–6.
- BLEVINS, R. 1990 *Flow-Induced Vibrations*. Van Nostrand Reinhold.
- BOURGUET, R. & JACONO, D. L. 2014 Flow-induced vibrations of a rotating cylinder. *J. Fluid Mech.* **740**, 342–380.
- BRADSHAW, P. & PANKHURST, R. C. 1964 The design of low-speed wind tunnels. *Prog. Aerosp. Sci.* **5**, 1–69.
- DOARÉ, O. & MICHELIN, S. 2011 Piezoelectric coupling in energy-harvesting fluttering flexible plates: linear stability analysis and conversion efficiency. *J. Fluids Struct.* **27** (8), 1357–1375.
- FUJISAWA, N., KAWAJI, Y. & IKEMOTO, K. 2001 Feedback control of vortex shedding from a circular cylinder by rotational oscillations. *J. Fluids Struct.* **15**, 23–27.
- GOVARDHAN, R. & WILLIAMSON, C. H. K. 2000 Modes of vortex formation and frequency response of a freely vibrating cylinder. *J. Fluid Mech.* **420**, 85–130.
- GOVARDHAN, R. N. & WILLIAMSON, C. H. K. 2006 Defining the modified Griffin plot in vortex-induced vibration: revealing the effect of Reynolds number using controlled damping. *J. Fluid Mech.* **561**, 147–180.
- GROUTHIER, C., MICHELIN, S. & DE LANGRE, E. 2013 Energy harvesting by vortex-induced vibrations in slender structures. In *ASME 2013 32nd International Conference on Ocean, Offshore and Arctic Engineering*, pp. V007T08A013–V007T08A013. American Society of Mechanical Engineers.
- JUNG, H. J. & LEE, S. W. 2011 The experimental validation of a new energy harvesting system based on the wake galloping phenomenon. *Smart Mater. Struct.* **20** (5), 055022.
- KARABELAS, S. J., KOUMROGLOU, B. C., ARGYROPOULOS, C. D. & MARKATOS, N. C. 2012 High Reynolds number turbulent flow past a rotating cylinder. *Appl. Math. Model.* **36** (1), 379–398.
- KHALAK, A. & WILLIAMSON, C. H. K. 1999 Motions, forces and mode transitions in vortex-induced vibrations at low mass-damping. *J. Fluids Struct.* **13** (7), 813–851.
- KLAMO, J. T. 2007 Effects of damping and Reynolds number on vortex-induced vibrations. Doctoral dissertation, California Institute of Technology.
- KOCABIYIK, S. & AL-MDALLAL, Q. M. 2005 Bluff-body flow created by combined rotary and translational oscillation. In *Fluid Structure Interaction and Moving Boundary Problems*, WIT Transactions on the Built Environment, vol. 84, pp. 195–203. WIT Press.
- LU, L., QIN, J., TENG, B. & LI, Y. 2011 Numerical investigations of lift suppression by feedback rotary oscillation of circular cylinder at low Reynolds number. *Phys. Fluids* **23**, 033601.
- MA, X., KARNIADAKIS, G. E., PARK, H. & GHARIB, M. 2003 DPIV-driven flow simulation: a new computational paradigm. *Proc. R. Soc. Lond. A* **459** (2031), 547–565.
- MITTAL, S. & KUMAR, B. 2003 Flow past a rotating cylinder. *J. Fluid Mech.* **476**, 303–334.
- MORSE, T. L., GOVARDHAN, R. N. & WILLIAMSON, C. H. K. 2008 The effect of end conditions on the vortex-induced vibration of cylinders. *J. Fluids Struct.* **24** (8), 1227–1239.
- MORSE, T. L. & WILLIAMSON, C. H. K. 2009 Fluid forcing, wake modes, and transitions for a cylinder undergoing controlled oscillations. *J. Fluids Struct.* **25** (4), 697–712.
- NAUDASCHER, E. & ROCKWELL, D. 1994 *Flow-Induced Vibrations: An Engineering Guide*. A. A. Balkema.
- NAZARINIA, M., LO JACONO, D., THOMPSON, M. C. & SHERIDAN, J. 2009a Flow behind a cylinder forced by a combination of oscillatory translational and rotational motions. *Phys. Fluids* **21** (5), 051701.

- NAZARINIA, M., LO JACONO, D., THOMPSON, M. C. & SHERIDAN, J. 2009b The three-dimensional wake of a cylinder undergoing a combination of translational and rotational oscillation in a quiescent fluid. *Phys. Fluids* **21** (6), 064101.
- PAIDOUSSIS, M. P., STUART, J. P. & DE LANGRE, E. 2011 *Fluid-Structure Interactions*. Cambridge University Press.
- PARKINSON, G. 1989 Phenomena and modelling of flow-induced vibrations of bluff bodies. *Prog. Aerosp. Sci.* **26** (2), 169–224.
- PRASNATH, T. K. & MITTAL, S. 2008 Vortex-induced vibrations of a circular cylinder at low Reynolds numbers. *J. Fluid Mech.* **594**, 463–491.
- SANCHEZ-SANZ, M., FERNANDEZ, B. & VELAZQUEZ, A. 2009 Energy-harvesting micro-resonator based on the forces generated by the Karman street around a rectangular prism. *J. Microelectromech. Syst.* **18**, 449–457.
- SARPKAYA, T. 2004 A critical review of the intrinsic nature of vortex-induced vibrations. *J. Fluids Struct.* **19** (4), 389–447.
- SARPKAYA, T. 2010 *Wave Forces on Offshore Structures*. Cambridge University Press.
- SEYED-AGHAZADEH, B. & MODARRES-SADEGHI, Y. 2015 An experimental investigation of vortex-induced vibration of a rotating circular cylinder in the crossflow direction. *Phys. Fluids* **27** (6), 067101.
- SINGH, K., MICHELIN, S. & DE LANGRE, E. 2012 Energy harvesting from axial fluid-elastic instabilities of a cylinder. *J. Fluids Struct.* **30**, 159–172.
- STANSBY, P. K. & RAINEY, R. C. T. 2001 On the orbital response of a rotating cylinder in a current. *J. Fluid Mech.* **439**, 87–108.
- STROUHAL, V. 1878 Uber eine besondere art der tonerregung. *Ann. Phys. Chem. New Series* **5**, 216–251.
- VICENTE-LUDLAM, D., BARRERO-GIL, A. & VELAZQUEZ, A. 2014 Optimal electromagnetic energy extraction from transverse galloping. *J. Fluids Struct.* **51**, 281–291.
- VICENTE-LUDLAM, D., BARRERO-GIL, A. & VELAZQUEZ, A. 2015 Enhanced mechanical energy extraction from transverse galloping using a dual mass system. *J. Sound Vib.* **339**, 290–303.
- VICENTE-LUDLAM, D., BARRERO-GIL, A. & VELAZQUEZ, A. 2017 Flow-induced vibration of a rotating circular cylinder using position and velocity feedback. *J. Fluids Struct.* **72**, 127–151.
- WILLIAMSON, C. H. K. & GOVARDHAN, R. 2004 Vortex-induced vibrations. *Annu. Rev. Fluid Mech.* **36**, 413–455.
- XU-XU, J., BARRERO-GIL, A. & VELAZQUEZ, A. 2016 Experimental study on transverse flow-induced oscillations of a square-section cylinder at low mass ratio and low damping. *Exp. Therm. Fluid Sci.* **74**, 286–295.